nature astronomy

Article

https://doi.org/10.1038/s41550-023-01936-8

Simultaneous space and phase resolved X-ray polarimetry of the Crab pulsar and nebula

Received: 29 July 2022

Accepted: 6 March 2023

Published online: 6 April 2023

Check for updates

A list of authors and their affiliations appears at the end of the paper

The Crab pulsar and its nebula are among the most studied astrophysical systems, and constitute one of the most promising environments where high-energy processes and particle acceleration can be investigated. They are the only objects for which significant X-ray polarization was detected in the past. Here we present the Imaging X-ray Polarimetry Explorer (IXPE) observation of the Crab pulsar and nebula. The total pulsar pulsed emission in the [2–8] keV energy range is unpolarized. Significant polarization up to 15% is detected in the core of the main peak. The nebula has a total space integrated polarized degree of 20% and polarization angle of 145°. The polarized maps show a large variation in the local polarization, and regions with a polarized degree up to 45–50%. The polarization pattern suggests a predominantly toroidal magnetic field. Our findings for the pulsar are inconsistent with most inner magnetospheric models, and suggest emission is more likely to come from the wind region. For the nebula, the polarization map suggests a patchy distribution of turbulence, uncorrelated with the intensity, in contrast with simple expectations from numerical models.

The Crab pulsar (PSR B0531+21, PSR J0534+2200) and nebula (G184.6-5.8), born out of the supernova SN1054, form one of the most interesting high-energy astrophysical systems, and one of the foremost environments where the physics of compact objects, particle acceleration and relativistic outflows can be investigated[1,2].

The Crab pulsar (PSR) and nebula (PWN) are the only astrophysical systems for which statistically significant integrated and/or phase resolved X-ray polarization was reported in the past by various instruments[3–11], suggesting that the polarization degree (PD) in the pulses, roughly 20%, is lower than in the interpulse. The integrated X-ray PD in the off pulse (OP) due to the PWN is consistently found to be roughly 20% with typical polarization angle (PA) of roughly 130–140°. The PWN polarimetry by OSO-8 has PD = 19.19 ± 0.97 and 19.50 ± 2.77% at 2.6 and 5.5 keV, respectively, while PA = 156.36 ± 1.44 and 152.99 ± 4.04°, at the same energies[3] (all errors hereafter are at the 1σ confidence level; Methods).

The Crab PWN has an apparent size of 6′ × 4′ in the optical band, about twice as large as in X-rays, corresponding to about 11 × 7 light yr at its estimated distance of 2 kpc (ref. 12). It has a broad band non-thermal spectrum, extending from radio to Tera eV (TeV) energies, due to synchrotron from high-energy electrons and positrons up to roughly 150 MeV, and Inverse Compton above. The [2–8] keV integrated luminosity is roughly 1.8×10^{-8} erg cm^{-2} s^{-1} (ref. 13) with a photon index of roughly 2.12–2.15 (ref. 14). X-ray imaging shows a well developed axisymmetric structure known as a jet torus[15,16]. Radio polarization shows typical average values of the PD in the range 5–10% and PA = 150°, with no correlation with the X-ray features[17]. High-resolution optical polarimetry of a few selected features in the inner region, within 10 arcsec from the PSR, shows a PD = 40% and PA = 127° (ref. 18).

The Crab PSR has a rotation period P = 33.7 ms, and spins down at a rate $\dot{P} = 4.21 \times 10^{-13}$ s s^{-1}, corresponding to an effective surface dipole magnetic field of 3.8×10^{12} G, and a spin-down luminosity $\dot{E} = 4.3 \times 10^{38}$ erg s^{-1} (ref. 2). Pulsed emission has been observed at all wavelengths from radio up to TeV. The pulse shape is characterized by a main pulse (P1), and an interpulse or second pulse (P2), whose positions in phase show only a slight variation with energy[19]. At optical

e-mail: niccolo.bucciantini@inaf.it

https://doi.org/10.1038/s41550-023-01936-8

frequencies and above, a bridge (B) of emission is observed between them. The total unabsorbed pulsed X-ray flux in the [2–10] keV band is roughly 2.7×10^{-9} erg cm^{-2} s^{-1} (ref. 20), while the photon index in the energy band [1–100] keV is found to vary in phase between 1.4 and 2.2 (ref. 21–24). The photon index is phase dependent: the emission is harder for B than for the peaks, and slightly harder for P2 than P1. Optical and radio polarization have been measured since the PSR discovery. The OP emission (in optical in the phase range 0.78–0.84) has a PD = 33% and PA = 130° (ref. 25). After OP subtraction, the average PD of the pulses is found to be 5.5% and the average PA is 96° (ref. 25).

Results

The Imaging X-ray Polarimetry Explorer (IXPE), the first mission devoted to spatially resolved polarization measurements in the X-rays[26,27], was successfully launched on 2 December 2021. IXPE observed the Crab PWN and PSR complex twice between 21 February and 7 March 2022 for a total on-source time of roughly 92 ks. Data were extracted and analysed according to standard procedures: HEASOFT v.6.30.1 (https://heasarc.gsfc.nasa.gov/docs/software/heasoft/) was used to perform a barycenter correction, with the BARYCORR FTOOL, using the most recent optical coordinates from the Gaia Data release 3, the DE421 JPL ephemeris and the ICRS reference frame (Supplementary Table 1). ixpeobssim v.26.3.2 was used to do energy calibration, detector World Coordinate System correction, aspect-solution corrections and all further (unweighted) analysis[28,29], including phase folding at the derived ephemeris. We also performed a coeval observation of the Crab PWN with the CHANDRA Satellite (ObdID 23539; see Methods for further details).

In Fig. 1 (Table 1) we show the polarized properties of the Crab complex derived by spatially integrating all emission in a region within 2.5 arcmin from the PSR. Background contamination within this region is negligible. There is a significant change in the PA between the low [2–4] keV and high [4–8] keV energy band. The same trend is seen for the OP emission (whose phase range can be found in Supplementary Table 2), suggesting that it is of nebular origin. The change in PD is less significant, with the higher energy band being slightly more polarized. The OP phase emission is marginally more polarized than the total PWN and PSR emission, as already suggested by a similar analysis of the OSO-8 data[3], while there is no evidence for even a marginal change in PA, suggesting that the PSR has a net low level of polarization, acting mostly to reduce the total level of polarization. The contribution of the PSR unpulsed (direct current) emission[30] to the total OP emission, is estimated to be less than 1% and we can safely assume that the OP is mostly of nebular origin (we found no evidence for variations of the polarization properties in the OP; Supplementary Fig. 1). The OP PA is roughly 145°, larger by roughly 20° with respect to the values reported in the literature for the PWN symmetry axis, derived from fitting the X-ray jet-torus intensity maps[26,31]. It is also smaller by roughly 10° than the previous OSO-8 measurements at a statistically significant level (Supplementary Fig. 2). Such discrepancies might simply reflect the variability of the PWN, where structures are known to change in shape and location over a typical time scale of a few years[32].

In Fig. 2 we show an intensity map of the Crab PWN from the coeval CHANDRA ObdID 23539, the IXPE count map for the PWN and PSR complex in the [2–8] keV energy range, and the IXPE count map in the same energy range, but computed just for the OP emission.

For the phase resolved analysis of the PSR we take events in the range [2–8] keV and within 20 arcsec from the PSR itself to limit the PWN contamination. The Stokes parameters of the OP emission have been subtracted (see Supplementary Material for the exact definition of the OP in terms of pulse phase, as well as the other phase bins). In Fig. 3 we plot the OP-subtracted light curve, in 200 equally spaced phase bins. For the polarization analysis of the PSR emission we opted for a variable phase binning, focusing on the peaks and bridge, to get a finer sampling near P1 and P2. Figure 3 shows PSR normalized Stokes

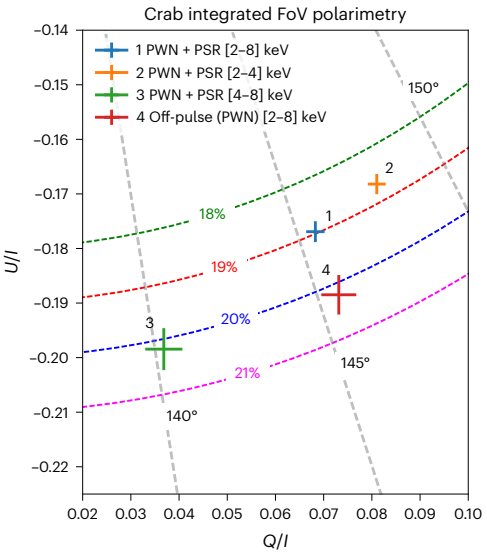

Fig. 1 | Global polarization properties of the Crab PWN + PSR complex. Emission is integrated over a region of 2.5; radius centred on the PSR. Normalized Stokes parameters are shown for the total emission, the emission in the [2–4] keV and [4–8] keV energy bands (mean values plus error bars representing the 1σ standard deviation) and for the OP only, together with contours of polarized degree (in %) and angle.

parameters U/I and Q/I, for the phase bins of interest (see Supplementary Table 2 for further details). The OP emission in the PSR aperture has $Q/I = -0.0106 \pm 0.008$, $U/I = -0.241 \pm 0.008$, corresponding to PD = 24.1% ± 0.8% and PA = 133.6 ± 1.0°. This is significantly more polarized than the OP emission for the entire PWN, and the PA is roughly 10° smaller, indicative of a spatial variation of the polarization properties. The only phase bin showing a polarization above the 3σ confidence level is the centre of P1 in the phase range [0.12,0.14], where the OP-subtracted emission has $Q/I = -0.132 \pm 0.025$, $U/I = -0.079 \pm 0.025$, corresponding to PD = 15.4 ± 2.5% and PA = 105 ± 18°. There is no significant change of the polarization properties of this phase bin with energy. Rapid PA variation might suppress the polarization in these bins. The total PSR normalized Stokes parameters are $Q/I = -0.018 \pm 0.019$ and $U/I = -0.019 \pm 0.019$, confirming that the integrated PSR contribution serves only to reduce the polarization of the entire complex.

In Fig. 4 we show the total PWN and PSR map of PD in the [2–8] keV energy range, obtained by smoothing the maps of Stokes parameters with a Gaussian kernel (5 arcsec width) and cut at the 5σ significance level (Supplementary Figs. 2 and 3), together with an intensity map where we have overlaid the polarized magnetic field direction (by definition perpendicular to direction of the electric field). We are able to map the magnetic field structure in the inner nebula. The overall polarization pattern confirms long-held general expectations for PWNe based on the paradigm that the synchrotron emission takes place in the (mostly) toroidal magnetic field, originating from the PSR wind and compressed in the nebula, which sets the symmetry axis of the jet torus structure. The observed polarization and emission patterns arise from the interplay of the magnetic field geometry and bulk motion of the relativistic plasma within the nebula itself, also depending on the inclination of the nebular axis with respect to the line of sight. It is indeed the presence of bulk motions directed towards and away from the observer that creates the various bright arc-like features and makes the front side of the torus brighter than the back. The results shown in Fig. 4 agree with this picture, assuming a symmetry axis inclined in the plane of the sky as derived from X-rays[31]. The direction of the inferred magnetic field broadly follows the shape of the emission torus (which extends also on the back but is fainter due to Doppler de-boosting). There are two unpolarized regions

https://doi.org/10.1038/s41550-023-01936-8

Table 1 | Global polarization properties of the PSR+PWN complex

Selection	*Q/I*	*U/I*	PD (%)	PA (degrees)	Significance
PSR+PWN [2–8] keV	0.177(0.0019)	0.068(0.0019)	19.0(0.19)	145.5(0.29)	99
PSR+PWN [2–4] keV	0.168(0.0019)	0.081(0.0019)	18.7(0.19)	147.8(0.29)	100
PSR+PWN [4–8] keV	0.199(0.0038)	0.037(0.0039)	20.2(0.38)	140.2(0.55)	53
PWN (OP)	0.189(0.0036)	0.073(0.0036)	20.2(0.36)	145.6(0.51)	57

Normalized Stokes parameters, polarized degree and angle for various energy and phase ranges (in brackets the 1σ errors). The OP is in the [2–8] keV range. The significance is given as the ratio of PD over its 1σ error (Fig. 1).

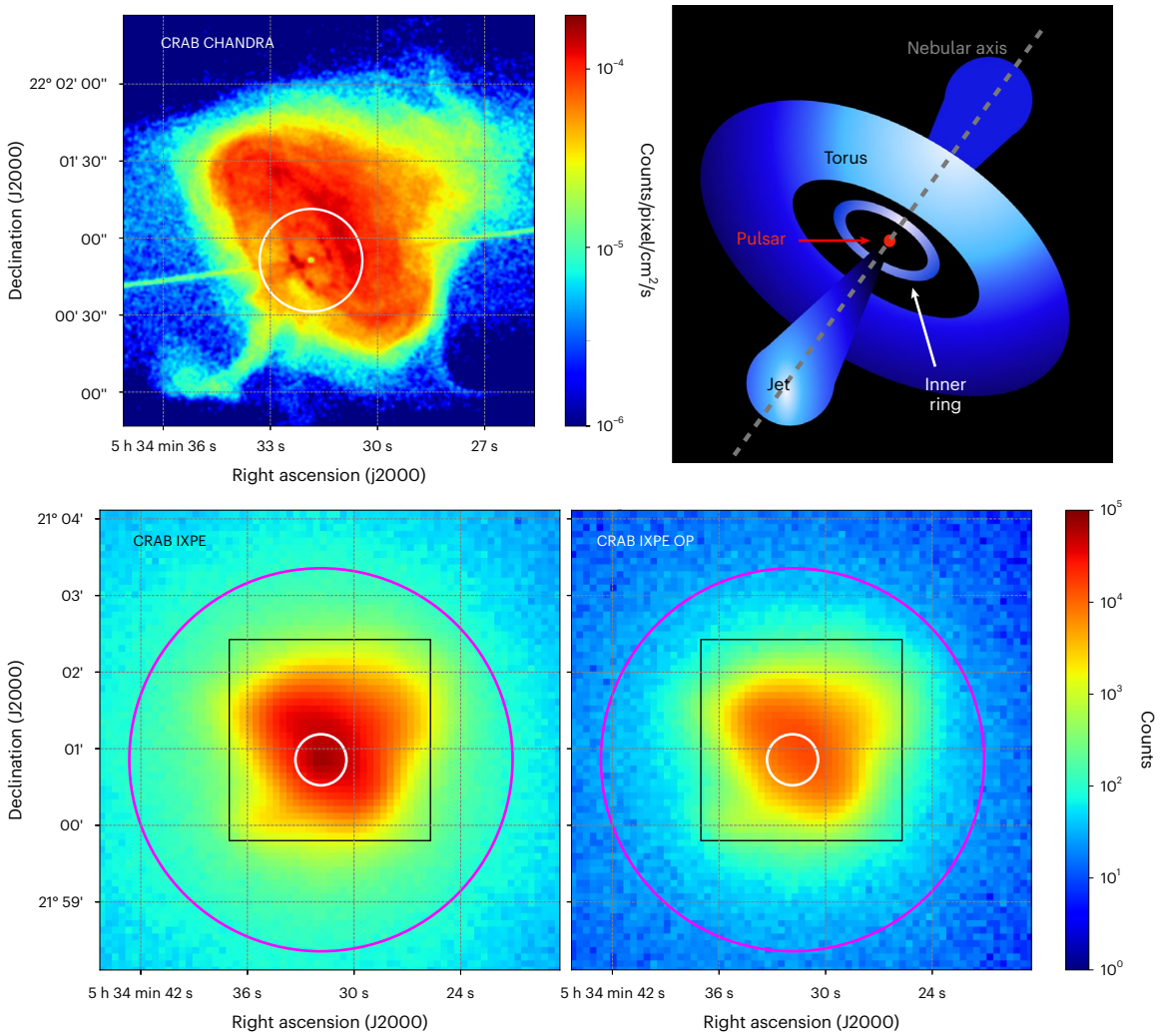

Fig. 2 | Comparison of Chandra and IXPE images. The top left panel shows the Chandra image (ObdID 23539) (intensity map) of the Crab PWN in the [2–8] keV energy range. The top right panel shows a cartoon of the jet torus structure indicating the main features observed in X-rays. The bottom left panel shows the total IXPE count map in the [2–8] keV energy range. The bottom right panel shows the OP (see Supplementary Materials for the definition of its phase range) only IXPE count map in the [2–8] keV energy range. The white circular region of 20′ radius is the one used to do the phase resolved polarimetry of the PSR. The magenta circular region of 2.5 arcmin radius is the one used for spatially integrated measures. The black box represents the region corresponding to the Chandra image.

at the north-east and south-west edges of the main torus, where the polarized direction varies rapidly within the point spread function. The overall PD map shows a far stronger level of asymmetry with respect to the PWN axis than the total intensity map, indicating possibly large variations in the amount of magnetic turbulence within the PWN, or major distortions of the magnetic field structure in the fainter outer regions. The more polarized regions are not found in the centre of the PWN, where there is a marginal contribution from the PSR that lowers the PD, but north and south of the main torus, in regions that do not correspond to any bright feature in X-ray. On the basis of smoothed maps the peak PD in the Northern region is found to be 46%, with a PA of 163°, at 25σ significance, while the peak in the southern region has PD of 51%, with a PA 156° at 20σ significance (Supplementary Fig. 3). Considering instead two circular regions of 15 arcsec radius centred on the polarization maxima, we found for the northern region integrated quantities: $Q/I = 0.37 \pm 0.01$ and $U/I = -0.25 \pm 0.01$, corresponding to PD $45 \pm 1\%$ and PA $163.3 \pm 0.8°$, at 35σ significance with a minimum detectable polarization (MDP) at 99% confidence level of 0.04, whereas the

https://doi.org/10.1038/s41550-023-01936-8

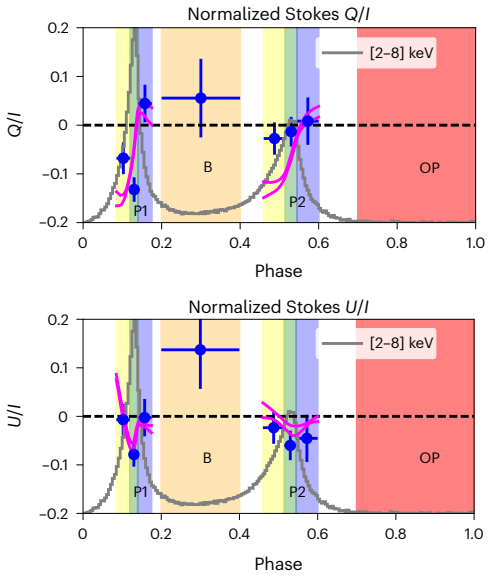

Fig. 3 | Polarization properties of the Crab PSR. Normalized Stokes parameters (means with vertical bar for their 1σ standard deviation) for the OP-subtracted emission of the Crab PSR in the [2–8] keV energy bands (blue crosses and the horizontal bar is the bin width), overlaid with the phase bins of interest: OP (red), P1 and P2 centres (green), left wings (yellow) and right wings (blue) and B (orange) (see Supplementary Materials for the definition of the various phase ranges). Overlaid is the OP-subtracted PSR light curve (counts) in the [2–8] keV energy band, normalized and rescaled to the range of the *y* axis (grey solid line). The magenta curves represent the range of optical data[25] over P1 and P2.

southern region has $Q/I = 0.30 \pm 0.02$, $U/I = -0.37 \pm 0.02$, corresponding to PD 47 ± 2% and PA = 154 ± 1°, at 27σ significance with a MDP of 0.05. These regions are far enough from the PSR that its depolarizing contribution is negligible.

Discussion

We report here a simultaneous phase and space-resolved soft X-ray polarized observation of the Crab PSR and PWN. Our results show that the total polarization of the pulsed signal is negligible. As can be seen from Fig. 3, the consistency with optical polarization measure[25] is marginal. Deviations are prominent for Q/I in the left wings of both P1 and P2. U/I on the other hand is in very good agreement. The discrepancy for P1 is an indication that the polarization swing observed in the optical range is not fast enough to match the X-ray trend. Note, however, that differences are below the 3σ uncertainty. Only the core of the main peak was found to be significantly polarized. This represents a statistically significant detection of an X-ray polarized signal from the Crab PSR. Marginal evidence for polarization, below 3σ, in other phase bins is also reported. The low average polarization is in contrast with most of the existing PSR models[33,34] that typically predict polarization fraction in the pulsed emission of 40–80%. The model polarization is generally especially high in the B phase bin. The peaks that are believed to be caustics are typically depolarized by means of rapid PA sweeps. By contrast, we find our highest PD in the core of P1. Moreover, a simple PA swing (at a constant rate over P1) does not seem capable by itself of explaining the presence of a highly polarized core in P1 surrounded by low polarization wings, unless the PA swings much faster than in the optical range. Intrinsic depolarization is most probably required. This is easily seen by comparing the Q/I trend as shown in Fig. 3. Hence the PD must vary across P1, and be intrinsically higher in the core. Analytical striped-wind emission models suggest possible lower polarization in B, but also predict a fully unpolarized P1 (ref. 34). However, recent models, focused on emission in the wind and outer magnetosphere and based on numerical magnetospheric solutions, have shown that the polarization signatures are highly sensitive to the location and geometry of the emission region[35,36]. Low integrated polarization suggests that the emission region should be close to or beyond the Light Cylinder[36]. However, none of the current models includes important physical ingredients: micro-turbulence, which is probably present in the wind current sheet[37] and could lead to significant depolarization; short time-scale variability that manifests as timing noise and could lead to potential depolarization for long time integration.

A detailed comparison with previous measures, typically in higher energy ranges, or with optical data would benefit from better statistics, and would require further modelling/extrapolation (to account for changes in the pulse shape with energy) and goes beyond the scope of this work. Thus we have chosen to avoid any discussion or comparison with earlier polarization measurements with statistical significance less than 3σ. Due to their large error bars, previous results[7,8] are compatible with our measures (Supplementary Fig. 1). The best estimates for the polarized fraction of the hard X-ray integrated PSR emission have typical values of roughly 20–30% (with low significance and and with some inconsistency among different observations). Given the low MDP (high sensitivity) of our measurement, we can confidently state that the PSR emission in the [2–8] keV must have an integrated polarized fraction of less than 20%. Note, however, that the more recent PolarLight narrow band [3–4.5] keV measures[10] are consistent with our findings that the PSR emission is probably unpolarized. A strong decrease in the PD of the total pulsed emission, from the optical to the soft X-ray (with a possible recovery to large PD in the hard X-ray) is not expected in existing modelling, which primarily relies on geometry of the emission zone to determine the polarization (for example, ref. 36); as noted above, additional physical effects will be required to accommodate the IXPE data.

We were able to map the large scale PWN polarization pattern confirming the general expectation of a predominantly toroidal magnetic field, extending well beyond the observed location of the X-ray torus. Indeed, earlier spatially resolved optical polarization measurements did not show unambiguously the presence of toroidal magnetic field. For synchrotron radiation, this is consistent with general expectation from magnetohydrodynamic modelling of this source[38–42]. We found, however, that the mostly symmetric PA (that is, magnetic field) pattern is associated with large asymmetries in the PD, probably indicating variations in the level of turbulence inside the PWN. Such a level of asymmetry is similar to, but stronger than, that seen in the intensity maps, and reflects a similar trend found in optical polarization images[2].

The magnetic axis of the PWN, derived by taking the symmetry axis of the magnetic field pattern, is found to be roughly 140°, about 15° further out than estimates based on fitting axisymmetric structure to the torus intensity[31]. It is also possible to estimate the inclination of the magnetic axis with respect to the plane of the sky: we found it to be roughly 60°, in agreement with previous estimates. While the average PD roughly 20% agrees with previous measures, the PA differs in a statistically significant way from other estimates, reflecting the spatial variation of the PD, or possible temporal variability. The spatially resolved PD reaches a maximum of roughly 46–50%. This is about two times larger than expected from simple predictions based on synchrotron turbulent modelling of the Crab Torus and Inner Ring luminosity profiles, calibrated on the OSO-8 results[42]. More sophisticate 3D models (lacking, however, micro-turbulence) can give PD values close to the theoretical maximum of roughly 70% (ref. 40), with higher values typically in the south-west region, but in general the prediction is for polarized patterns symmetric with respect to the nebular axis, unlike what was found. This suggests that the level and development of turbulence within the nebula is not as strong as predicted[42] and much patchier in its spatial distribution. While the lower level of polarization close to the centre of the PWN is easily explained by summed emission from a wide range of PA in the central resolution elements, the increase of the PD with distance at the rim of the torus suggests the presence of a highly ordered magnetic layer at the edge of the torus itself (the ratio of

https://doi.org/10.1038/s41550-023-01936-8

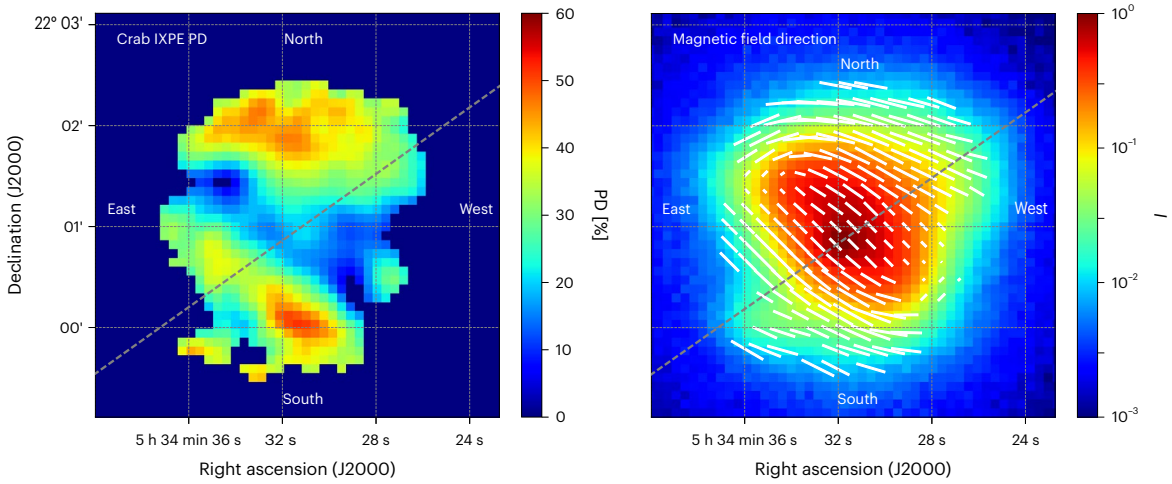

Fig. 4 | Polarized structure of the Crab nebula. The right panel shows the total intensity map of the Crab PWN + PSR complex in the [2–8] keV energy band, overlaid with the reconstructed polarization direction (magnetic field). The left panel shows a map of the PD cut above 5σ confidence level. The grey dashed line is the nebular axis inferred from X-ray intensity maps[31]. Overlaid are the sky directions for ease of reference.

the energy in the turbulent versus ordered magnetic field components should be about a factor of two smaller than in the core of the torus[43]). This differs from what is seen in optical where higher polarization is found in a few selected inner features[18], suggesting that optical and X-ray emitting particles might be accelerated in different locations and sample different regions of the nebula as previously claimed[32]. Note, however, that the X-ray inner ring, which supposedly traces the wind termination shock, at the same distance of the optical wisps (smaller than the IXPE resolution), is strongly subdominant with respect to the torus (and the PSR), such that, even if highly polarized, it would not give a significant signal. The fact that the PD (which depends on the ratio of magnetic energy in the turbulent to ordered components) is far more asymmetric, with respect to the nebular axis, than the intensity (which depends on the total turbulent plus ordered magnetic energy density) suggests that the level of turbulence anticorrelates with the strength of the ordered component of the magnetic field. This is what one would expect if turbulence was driven by the growth of instabilities, such as Rayleigh–Taylor, which are suppressed by stronger fields[44]. If this is correct, we should expect that more highly polarized PWNe (less turbulent systems) should show a stronger toroidal patterns with smaller degree of Rayleigh–Taylor induced patchy depolarization and intensity enhancement.

The IXPE polarization results indicate that present modelling lacks physical ingredients needed to explain the low PSR polarization seen at most phases. The substantial spatial variation of the PD in the nebula also indicates that effects are missing even in the most advanced 3D relativistic magneto-hydrodynamical models; magnetohydrodynamic turbulence seems likely to be important in both cases.

Methods

Observations and data analysis

The IXPE is a National Aeronautics and Space Administration (NASA) mission in partnership with the Italian Space Agency (ASI) launched in 9 December 2021. As described in detail elsewhere (refs. 26,27 and references therein), the IXPE Observatory includes three identical X-ray telescopes (DUs), each comprising a Wolter-I X-ray mirror assembly (NASA-provided) with angular resolution (half-power diameter) of 19 (DU1), 26 (DU2), 28 (DU3) arcsec, respectively, and a polarization-sensitive pixelated detector (gas pixel detector (GPD), ASI-provided), with a typical energy-dependent dead time of roughly 1.1 ms. This allows one to measure the energy, arrival direction, arrival time and linear polarization of the detected X-ray signal, which are all reconstructed from the photo-electron track shape using moment analysis. The IXPE energy range is the [2–8] keV band, with a total effective area of 590 cm^2 at 4.5 keV. The modulation factor (the amplitude of the modulation of the reconstructed photo-electrons angle distribution for a 100% polarized source) ranges from roughly 15% at 2 keV up to around 60% at 8 keV (ref. 27).

The Crab PWN and PSR were observed twice: the first time from 21 February 2022 UTC 16:13:32 to 22 February 2022 UTC 18:46:37, the second from 7 March 2022 UTC 00:14:20 to 8 March 2022 UTC 02:40:02, for a total of 92,363 s of ONTIME exposure (the total exposure as obtained from the sum of the good time intervals) and 85,062 s of total LIVETIME (the total amount of time in which the charge-coupled device was actively observing a source; this excludes the time it takes to transfer charge from the image region to the frame store region).

We carried out the polarization analysis on publicly available level 2 event list files. These were corrected to account for the following calibration issues that have emerged during flight operations. The World Coordinate System was corrected to account for the small offset among the various units, registering the pointing solution to centre the intensity peak of each unit on the PSR position at right ascension = 5 h 34 min 31.86 s, declination = 22° 00′ 51.3". The time dependent charge-to-energy conversion was reconstructed for each units using the two onboard calibration sources at 1.7 keV (Si Kα) and 5.9 keV (^{55}Fe → ^{55}Mg with following Kα emission)[45]. Spurious offsets in the pointing solution (aspect solution), associated with the switch between different star trackers during orbit, were identified looking at the time variations of the count rate in a set of background sky regions and later filtered out by removing the affected time intervals. This results in a loss of counts smaller than 2% and an effective new on-source time of roughly 91 ks. At the time of the Crab observation, the optical axis of the mirror system relative to the star trackers had not yet been accurately determined and was not yet compensated (by offset pointing). Consequently, the Crab PSR was about 2.8 arcmin off axis with respect to the mirror system. This precluded accurate computation of image response functions—energy-dependent vignetting and energy-dependent exposure maps—necessary for a correct spectral analysis (the mirror-system–star-tracker offset has now been accurately determined and compensated, such that future observations will place the image close to the mirror-system optical axis. Furthermore, it may be possible, in the future, to recalibrate the image response functions) and for computing correct count rates. However, this should not affect polarization measures that come from flux ratios among Stokes parameters.

Timing analysis

We initially used the Jodrell Bank Crab PSR Monthly ephemeris (http://www.jb.man.ac.uk/pulsar/crab.html)[46] to calculate the pulse phase of each photon. However, the time span of the two IXPE observations requires two separate JB solutions, and the alignment between the arrival time of the pulse in the two observations using these ephemerides is visibly off (roughly 0.02 in phase). Therefore, we determined a new ephemeris by using the X-ray data alone, as follows. As a starting point, we used the JB monthly ephemeris of February in CGRO format (https://www.jb.man.ac.uk/~pulsar/crab/CGRO_format.html), but modifying the frequency and derivatives for them to refer to an epoch between the two observations:

$$\nu_{\rm new} = \nu_{\rm old} + \dot{\nu}_{\rm old}(T_{\rm new} - T_{\rm old}) + 0.5\ddot{\nu}_{\rm old}(T_{\rm new} - T_{\rm old})^2 \quad (1)$$

$$\dot{\nu}_{\rm new} = \ddot{\nu}_{\rm old}(T_{\rm new} - T_{\rm old}) \quad (2)$$

where $\nu_{\rm old}$, $\dot{\nu}_{\rm old}$ and $\ddot{\nu}_{\rm old}$ are the frequency, its first and second time derivative at $T_{\rm old}$, while $\nu_{\rm new}$ and $\dot{\nu}_{\rm new}$ are the frequency and its first time derivative at $T_{\rm new}$.

Then, we calculated times of arrival (TOAs) of the pulse using the HENphaseogram tool distributed with HENDRICS (https://hendrics.stingray.science)[47]. This tool folds the data in small fractions of the observation, creating a series of pulse profiles. Next, it calculates the misalignment between each of these profiles and a smoothed version of the folded profile from the whole observation, and transforms this misalignment into a TOA. The TOA refers to the maximum of the reference profile. As an output, the tool produces a parameter file and a TOA file in Tempo2 format[48]. We loaded these approximate parameters and TOAs in the pintk graphical interface to PINT (https://nanograv-pint.readthedocs.io)[49], and fitted a new spin-down solution that aligned the TOAs of the two observations. Then, we went back and calculated new TOAs, this time using the improved timing solution and, consequently, the better resolved total pulse profile that the solution provided, and fitted these TOAs again with PINT. We stopped this iterative procedure when the improvement in the fitting through PINT was smaller than the uncertainties. Finally, we calculated the closest TOA to the epoch chosen for the timing solution, and referred the frequency and derivatives to this time, using the above equation, to have a single number for the reference TOA and the PEPOCH of the timing solution for convenience. The new ephemeris is reported in Supplementary Table 1. Note that, having chosen the reference time in between the February and March observations, the determination of the second time derivative of the period is highly uncertain, but on the other hand the correction due to the second time derivative is not significant, and can potentially be neglected. Note, moreover, that the absolute time alignment of the pulse profile is not necessary for the analysis in this paper. However, we did verify that the X-ray pulse leads the radio pulse (as provided by the JB ephemeris) by roughly 300 μs, consistent with past observations from other missions[50]. The Crab PSR is a young one and its timing can be noisy, to the point that ephemeris cannot be extended beyond their range of validity.

Polarization analysis

The polarization analysis of both the PWN and the PSR was performed using the IXPE collaboration software ixpeobssim v.26.3.2. ixpeobssim has been designed to act both as a simulation software and for data reduction. We opted for a more robust and established unweighted analysis, limited to the [2–8] keV energy range. Phase folding was performed with xpphase, while event selection was done using the xpselect tool. Polarization was computed with the xpbin tool and PCUBE and PMAPCUBE methods.

Given the additive nature of Stokes parameters, to get the polarization properties of a spatial region and/or phase range of interest, we just need to take the sum of U and Q of each event (calibrated for the known spurious modulation of the instrument and corrected for the modulation factor[27]) within the same region and/or phase range. ixpeobssim can compute all polarization relevant quantities including their error and the significance. Deformation of the phase resolved light curve (pulse shape) due to dead time, with respect to the dead-time corrected one, is estimated to be less than 3% (the difference between the dead-time correction when the count rate is at maximum (P1) and the one when the count rate is at minimum (OP)), and was thus ignored. The net PSR's Stokes parameters in a given phase bin are obtained as follows: for a generic Stokes parameter $X(=I, U, Q)$ of phase bin i we have $X_{\rm op-sub,}{}_i = X_{{\rm tot},i} - X_{\rm OP}(\Delta_{{\rm phase},i}/\Delta_{\rm phase,OP})$, where $\Delta_{{\rm phase},i}$ is the phase width of phase bin i and $\Delta_{\rm phase,OP}$ is the phase width of OP bin (0.3). Supplementary Fig. 4 shows the maps of normalized Stokes parameters, of the total PWN plus PSR emission. The contribution of the lowly polarized PSR is hardly visible. We verified that the pattern, apart from counting noise, is the same if one considers just the emission in the OP phase range. Whereas the U/I map shows a high level of symmetry with respect to the direction of the nebular axis inferred from the intensity maps[31], the one for Q/I is far more asymmetric (its symmetry axis is more aligned with the north–south direction). The inclination of the magnetic axis of the nebula was derived by fitting ellipses to the internal magnetic field structure as shown in Fig. 4.

Owing to the brightness of the Crab Complex, all the IXPE field of view (FoV) contains events from the PSR and PWN; however, for space integrated measures, we have verified that polarization properties do not change once one selects a circular region centred on the PSR and with radius of more than 2 arcmin (we selected 2.5 arcmin). Supplementary Fig. 5 shows that roughly 98% of counts are within 2 arcmin. For the PSR analysis, we have verified, using a large set of mocked observations, that the optimal region size, to reduce the errors of the OP-subtracted polarization measures, ranges between 15 and 25 arcsec. We opted for 20 arcsec (Supplementary Fig. 5).

We caution the reader that due to error in the reconstruction of the photons absorption point in the GPD, polarization leakage can contaminate the Stokes maps. The effect of polarization leakage arises specifically from correlations between the reconstructed PA and the photon absorption point in the GPD. This leads to false polarization patterns (this has no effect on integrated or OP-subtracted values), even for unpolarized sources. Preliminary estimates based on Monte Carlo simulations of the GPD response indicate that this effect can at most be as high as 10% in the outer regions of the PWN, and does not alter significantly our overall findings. A more detailed discussion and treatment of this effect will be presented in a forthcoming publication.

CHANDRA observation

The Crab PWN was observed by CHANDRA (OsbID 23539) starting on 15 March 2022 at 11:32:23 UTC and ending on 15 March 2022 at 15:14:17 UTC, for a total of roughly 10^4 s; due to telemetry saturation from the bright source, the effective exposure time was 1,331 s. Data were processed with the CIAO package v.4.14 using CALDB v.4.9.7, with the chandra repro mode=h tool using default settings, and the [2–8] keV image was done with the fluximage tool, and later smoothed with a gaussian kernel using aconvolve kernelspec='lib:gaus(2,5,1,1,1)'.

Data availability

Data from the Crab PSR and nebula observation are available in the HEASARC IXPE Data Archive (https://heasarc.gsfc.nasa.gov/docs/ixpe/archive/). Additional data are available in the Supplementary Information and from figshare at https://doi.org/10.6084/m9.figshare.22203163. Source data are provided with this paper.

Code availability

The ixpeobssim software and documentation can be downloaded at https://github.com/lucabaldini/ixpeobssim. Other information supporting the findings of this study, and specific data-reduction pipelines, are available from the corresponding author upon request.

References

1. Gaensler, B. M. & Slane, P. O. The evolution and structure of pulsar wind nebulae. *Annu. Rev. Astron. Astrophys.* **44**, 17–47 (2006).
2. Hester, J. J. The Crab nebula: an astrophysical chimera. *Annu. Rev. Astron. Astrophys.* **46**, 127–155 (2008).
3. Weisskopf, M. C., Silver, E. H., Kestenbaum, H. L., Long, K. S. & Novick, R. A precision measurement of the X-ray polarization of the Crab nebula without pulsar contamination. *Astrophys. J. Lett.* **220**, L117–L121 (1978).
4. Forot, M., Laurent, P., Grenier, I. A., Gouiffès, C. & Lebrun, F. Polarization of the Crab pulsar and nebula as observed by the INTEGRAL/IBIS telescope. *Astrophys. J. Lett.* **688**, L29–L32 (2008).
5. Moran, P. et al. Optical polarimetry of the inner Crab nebula and pulsar. *Mon. Not. R. Astron. Soc.* **433**, 2564–2575 (2013).
6. Chauvin, M., Roques, J. P., Clark, D. J. & Jourdain, E. Polarimetry in the hard X-ray domain with INTEGRAL SPI. *Astrophys. J.* **769**, 137 (2013).
7. Chauvin, M. et al. Shedding new light on the Crab with polarized X-rays. *Sci. Rep.* **7**, 7816 (2017).
8. Vadawale, S. V. et al. Phase-resolved X-ray polarimetry of the Crab pulsar with the AstroSat CZT imager. *Nat. Astron.* **2**, 50–55 (2018).
9. Feng, H. et al. Re-detection and a possible time variation of soft X-ray polarization from the Crab. *Nat. Astron.* **4**, 511–516 (2020).
10. Long, X. et al. X-ray polarimetry of the Crab nebula with polarlight: polarization recovery after the glitch and a secular position angle variation. *Astrophys. J. Lett.* **912**, L28 (2021).
11. Li, H.-C. et al. Gamma-ray polarimetry of the Crab pulsar observed by POLAR. *Mon. Not. R. Astron. Soc.* **512**, 2827–2840 (2022).
12. Trimble, V. The distance to the Crab nebula and NP 0532. *Publ. Astron. Soc. Pac.* **85**, 579 (1973).
13. Kargaltsev, O. et al. in *40 Years of Pulsars: Millisecond Pulsars, Magnetars and More* Vol. 983 (eds Bassa, C. G. et al.) 171–185 (American Institute of Physics, 2008).
14. Mori, K. et al. Spatial variation of the X-ray spectrum of the Crab nebula. *Astrophys. J.* **609**, 186–193 (2004).
15. Hester, J. J. et al. WFPC2 studies of the Crab nebula. I. HST and ROSAT imaging of the synchrotron nebula. *Astrophys. J.* **448**, 240–263 (1995).
16. Weisskopf, M. C. et al. Discovery of spatial and spectral structure in the X-ray emission from the Crab nebula. *Astrophys. J. Lett.* **536**, L81–L84 (2000).
17. Aumont, J. et al. Measurement of the Crab nebula polarization at 90 GHz as a calibrator for CMB experiments. *Astron. Astrophys.* **514**, A70 (2010).
18. Moran, P. et al. Optical polarimetry of the inner Crab nebula and pulsar. *Mon. Not. R. Astron. Soc.* **433**, 2564–2575 (2013).
19. Zanin, R. in *Modelling Pulsar Wind Nebulae* Vol. 446 (ed. Torres, D. F.) 101–133 (Springer, 2017).
20. Kaaret, P. et al. Chandra observations of the Young pulsar PSR B0540-69. *Astrophys. J.* **546**, 1159–1167 (2001).
21. Massaro, E., Campana, R., Cusumano, G. & Mineo, T. The optical to γ-ray emission of the Crab pulsar: a multicomponent model. *Astron. Astrophys.* **459**, 859–870 (2006).
22. Weisskopf, M. C. et al. Chandra phase-resolved X-ray spectroscopy of the Crab pulsar. *Astrophys. J.* **743**, 139 (2011).
23. Ge, M. Y. et al. X-ray phase-resolved spectroscopy of PSRs B0531+21, B1509-58, and B0540-69 with RXTE. *Astrophys. J. Suppl. Ser.* **199**, 32 (2012).
24. Vivekanand, M. Phase-resolved spectrum of the Crab pulsar from NICER. *Astron. Astrophys.* **649**, A140 (2021).
25. Słowikowska, A., Kanbach, G., Kramer, M. & Stefanescu, A. Optical polarization of the Crab pulsar: precision measurements and comparison to the radio emission. *Mon. Not. R. Astron. Soc.* **397**, 103–123 (2009).
26. Weisskopf, M. The Imaging X-ray Polarimetry Explorer (IXPE) mission overview, in the AAS High Energy Astrophysics Division meeting. *Bulletin Am. Astr. Soc.* **54**, 301.01 (2022).
27. Weisskopf, M. C. et al. Imaging X-ray Polarimetry Explorer: prelaunch. *J. Astron. Telesc. Instrum. Syst.* **8**, 026002 (2022).
28. Pesce-Rollins, M., Lalla, N. D., Omodei, N. & Baldini, L. An observation-simulation and analysis framework for the Imaging X-ray Polarimetry Explorer (IXPE). *Nucl. Inst. Meth. Phys. Res. A* **936**, 224–226 (2019).
29. Baldini, L. et al. ixpeobssim: a simulation and analysis framework for the Imaging X-ray Polarimetry Explorer. *SoftwareX* **19**, 101194 (2022).
30. Tennant, A. F. et al. Discovery of X-ray emission from the crab pulsar at pulse minimum. *Astrophys. J. Lett.* **554**, L173–L176 (2001).
31. Ng, C.-Y. & Romani, R. W. Fitting pulsar wind tori. *Astrophys. J.* **601**, 479–484 (2004).
32. Schweizer, T. et al. Characterization of the optical and X-ray properties of the north-western wisps in the Crab nebula. *Mon. Not. R. Astron. Soc.* **433**, 3325–3335 (2013).
33. Dyks, J. & Harding, A. K. Rotational sweepback of magnetic field lines in geometric models of pulsar radio emission. *Astrophys. J.* **614**, 869–880 (2004).
34. Pétri, J. Phase-resolved polarization properties of the pulsar striped wind synchrotron emission. *Mon. Not. R. Astron. Soc.* **434**, 2636–2644 (2013).
35. Cerutti, B., Mortier, J. & Philippov, A. A. Polarized synchrotron emission from the equatorial current sheet in gamma-ray pulsars. *Mon. Not. R. Astron. Soc.* **463**, L89–L93 (2016).
36. Harding, A. K. & Kalapotharakos, C. Multiwavelength polarization of rotation-powered pulsars. *Astrophys. J.* **840**, 73 (2017).
37. Cerutti, B., Philippov, A. A. & Dubus, G. Dissipation of the striped pulsar wind and non-thermal particle acceleration: 3D PIC simulations. *Astron. Astrophys.* **642**, A204 (2020).
38. Bucciantini, N., del Zanna, L., Amato, E. & Volpi, D. Polarization in the inner region of pulsar wind nebulae. *Astron. Astrophys.* **443**, 519–524 (2005).
39. Nakamura, Y. & Shibata, S. Polarization of the Crab nebula with disordered magnetic components. *Mon. Not. R. Astron. Soc.* **381**, 1489–1498 (2007).
40. Porth, O., Komissarov, S. S. & Keppens, R. Three-dimensional magnetohydrodynamic simulations of the Crab nebula. *Mon. Not. R. Astron. Soc.* **438**, 278–306 (2014).
41. Olmi, B., Del Zanna, L., Amato, E., Bucciantini, N. & Mignone, A. Multi-D magnetohydrodynamic modelling of pulsar wind nebulae: recent progress and open questions. *J. Plas. Phys.* **82**, 635820601 (2016).
42. Bucciantini, N., Bandiera, R., Olmi, B. & Del Zanna, L. Modeling the effect of small-scale magnetic turbulence on the X-ray properties of pulsar wind nebulae. *Mon. Not. R. Astron. Soc.* **470**, 4066–4074 (2017).
43. Bandiera, R. & Petruk, O. Radio polarization maps of shell-type supernova remnants—I. Effects of a random magnetic field component and thin-shell models. *Mon. Not. R. Astron. Soc.* **459**, 178–198 (2016).
44. Bucciantini, N., Amato, E., Bandiera, R., Blondin, J. M. & Del Zanna, L. Magnetic Rayleigh-Taylor instability for pulsar wind nebulae in expanding supernova remnants. *Astron. Astrophys.* **423**, 253–265 (2004).
45. Ferrazzoli, R. et al. In-flight calibration system of Imaging X-ray Polarimetry Explorer. *J. Astron. Telesc. Instrum. Syst.* **6**, 048002 (2020).
46. Lyne, A. G., Pritchard, R. S. & Graham-Smith, F. 23 years of Crab pulsar rotational history. *Mon. Not. R. Astron. Soc.* **265**, 1003–1012 (1993).

47. Bachetti, M. HENDRICS: High ENergy Data Reduction Interface from the Command Shell. Record ascl:1805.019 (Astrophysics Source Code Library, 2018).
48. Hobbs, G. B., Edwards, R. T. & Manchester, R. N. TEMPO2, a new pulsar-timing package—I. An overview. *Mon. Not. R. Astron. Soc.* **369**, 655–672 (2006).
49. Luo, J. et al. PINT: a modern software package for pulsar timing. *Astrophys. J.* **911**, 45 (2021).
50. Kuiper, L., Hermsen, W., Walter, R. & Foschini, L. Absolute timing with IBIS, SPI and JEM-X aboard INTEGRAL. Crab main-pulse arrival times in radio, X-rays and high-energy gamma -rays. *Astron. Astrophys.* **411**, L31–L36 (2003).

Acknowledgements

The IXPE is a joint US and Italian mission. The US contribution is supported by NASA and led and managed by its Marshall Space Flight Center (MSFC), with industry partner Ball Aerospace (contract no. NNM15AA18C). The Italian contribution is supported by the Italian Space Agency (Agenzia Spaziale Italiana, ASI) through contract no. ASI-OHBI-2017-12-I.0, agreement nos. ASI-INAF-2017-12-H0 and ASI-INFN-2017.13-H0, and its Space Science Data Center (SSDC) with agreement nos. ASI-INAF-2022-14-HH.0 and ASI-INFN 2021-43-HH.0, and by the Istituto Nazionale di Astrofisica (INAF) and the Istituto Nazionale di Fisica Nucleare (INFN) in Italy. This research used data products provided by the IXPE Team (MSFC, SSDC, INAF and INFN) and distributed with additional software tools by the High-Energy Astrophysics Science Archive Research Center (HEASARC), at NASA Goddard Space Flight Center (GSFC). The research at Boston University was supported in part by National Science Foundation grant no. AST-2108622. Part of the French contributions is supported by the Scientific Research National Center (CNRS) and the French spatial agency (CNES). I.A. acknowledges financial support from the Spanish 'Ministerio de Ciencia e Innovación' (grant no. MCIN/AEI/10.13039/501100011033) through the Center of Excellence Severo Ochoa award for the Instituto de Astrofísica de Andalucía-CSIC (grant no. CEX2021-001131-S), and through grant nos. PID2019-107847RB-C44 and PID2022-139117NB-C44. C.-Y.N. is supported by a GRF grant from the Hong Kong Government under no. HKU 17305419. N.B. was supported by the INAF MiniGrant 'PWNnumpol - Numerical Studies of Pulsar Wind Nebulae in The Light of IXPE'. J.H. acknowledges support from the Natural Sciences and Engineering Research Council of Canada through a Discovery Grant, the Canadian Space Agency through the co-investigator grant programme, and computational resources and services provided by Compute Canada, Advanced Research Computing at the University of British Columbia, and the SciServer science platform. S.G. and E.W. were supported by grant nos. JSPS KAKENHI JP 19H00696 and 22K14068.

Author contributions

N.B. led the data analysis and the writing of the paper. R.F., M.B., J.R., L.P. and F.M. contributed to data analysis and data calibration. N.D.L., C.S., N.O., T.K., T.M., S.G. and E.W. contributed to data analysis and results interpretation. M.C.W., M.N., S.S., E.D.O.W., F.X., J.H., R.W.R., P.T., A.P. and H.L.M. contributed to text revision and data interpretation. L.B. and M.P.-R. contributed to software development. The remaining members of the IXPE collaboration contributed to the design of the mission, to the calibration of the instrument, to defining its science case and to the planning of the observations. All authors provided inputs and comments on the paper.

Competing interests

The authors declare no competing interests.

Additional information

Supplementary information The online version contains supplementary material available at https://doi.org/10.1038/s41550-023-01936-8.

Correspondence and requests for materials should be addressed to Niccolò Bucciantini.

Peer review information *Nature Astronomy* thanks Santosh Vadawale and the other, anonymous, reviewer(s) for their contribution to the peer review of this work.

Niccolò Bucciantini[1,2,3] ✉, Riccardo Ferrazzoli[4], Matteo Bachetti[5], John Rankin[4], Niccolò Di Lalla[6], Carmelo Sgrò[7], Nicola Omodei[6], Takao Kitaguchi[8], Tsunefumi Mizuno[9], Shuichi Gunji[10], Eri Watanabe[10], Luca Baldini[7,11], Patrick Slane[12], Martin C. Weisskopf[13], Roger W. Romani[6], Andrea Possenti[5], Herman L. Marshall[14], Stefano Silvestri[7], Luigi Pacciani[4], Michela Negro[15,16,17], Fabio Muleri[4], Emma de Oña Wilhelmi[18], Fei Xie[4,19], Jeremy Heyl[20], Melissa Pesce-Rollins[7], Josephine Wong[6], Maura Pilia[5], Iván Agudo[21], Lucio A. Antonelli[22,23], Wayne H. Baumgartner[13], Ronaldo Bellazzini[7], Stefano Bianchi[24], Stephen D. Bongiorno[13], Raffaella Bonino[25,26], Alessandro Brez[7], Fiamma Capitanio[4], Simone Castellano[7], Elisabetta Cavazzuti[27], Chien-Ting Chen[28], Stefano Ciprini[23,29], Enrico Costa[4], Alessandra De Rosa[4], Ettore Del Monte[4], Laura Di Gesu[27], Alessandro Di Marco[4], Immacolata Donnarumma[27], Victor Doroshenko[30], Michal Dovčiak[31], Steven R. Ehlert[13], Teruaki Enoto[8], Yuri Evangelista[4], Sergio Fabiani[4], Javier A. Garcia[32], Kiyoshi Hayashida[33], Wataru Iwakiri[34], Svetlana G. Jorstad[35,36], Philip Kaaret[37], Vladimir Karas[31], Fabian Kislat[38], Jeffery J. Kolodziejczak[13], Henric Krawczynski[39], Fabio La Monaca[4], Luca Latronico[25], Ioannis Liodakis[40], Simone Maldera[25], Alberto Manfreda[7], Frédéric Marin[41], Andrea Marinucci[27], Alan P. Marscher[35], Francesco Massaro[25,26], Giorgio Matt[24], Ikuyuki Mitsuishi[42], C.-Y. Ng[43], Stephen L. O'Dell[13], Chiara Oppedisano[25], Alessandro Papitto[22], George G. Pavlov[44], Abel L. Peirson[6], Matteo Perri[22,23], Pierre-Olivier Petrucci[45], Juri Poutanen[46],

Simonetta Puccetti[23], Brian D. Ramsey[13], Ajay Ratheesh[4], Oliver J. Roberts[28], Paolo Soffitta[4], Gloria Spandre[7], Doug Swartz[28], Toru Tamagawa[8], Fabrizio Tavecchio[47], Roberto Taverna[48], Yuzuru Tawara[42], Allyn F. Tennant[13], Nicolas E. Thomas[13], Francesco Tombesi[17,28,49], Alessio Trois[5], Sergey Tsygankov[46], Roberto Turolla[48,50], Jacco Vink[51], Kinwah Wu[50] & Silvia Zane[50]

[1]INAF Osservatorio Astrofisico di Arcetri, Florence, Italy. [2]Dipartimento di Fisica e Astronomia, Università degli Studi di Firenze, Sesto Fiorentino, Italy. [3]Istituto Nazionale di Fisica Nucleare, Sezione di Firenze, Sesto Fiorentino, Italy. [4]INAF Istituto di Astrofisica e Planetologia Spaziali, Rome, Italy. [5]INAF Osservatorio Astronomico di Cagliari, Selargius, Italy. [6]Department of Physics and Kavli Institute for Particle Astrophysics and Cosmology, Stanford University, Stanford, CA, USA. [7]Istituto Nazionale di Fisica Nucleare, Sezione di Pisa, Pisa, Italy. [8]RIKEN Cluster for Pioneering Research, Wako, Japan. [9]Hiroshima Astrophysical Science Center, Hiroshima University, Higashi-Hiroshima, Japan. [10]Yamagata University, Yamagata-shi, Japan. [11]Dipartimento di Fisica, Università di Pisa, Pisa, Italy. [12]Center for Astrophysics, Harvard Smithsonian, Cambridge, MA, USA. [13]NASA Marshall Space Flight Center, Huntsville, AL, USA. [14]MIT Kavli Institute for Astrophysics and Space Research, Massachusetts Institute of Technology, Cambridge, MA, USA. [15]Center for Research and Exploration in Space Science and Technology, NASA/GSFC, Greenbelt, MD, USA. [16]NASA Goddard Space Flight Center, Greenbelt, MD, USA. [17]Department of Astronomy, University of Maryland, Maryland, MD, USA. [18]Deutsches Elektronen-Synchrotron (DESY), Zeuthen, Germany. [19]Guangxi Key Laboratory for Relativistic Astrophysics, School of Physical Science and Technology, Guangxi University, Nanning, China. [20]University of British Columbia, Vancouver, British Columbia, Canada. [21]Instituto de Astrofísica de Andalucía, IAA-CSIC, Glorieta de la Astronomía s/n, Granada, Spain. [22]INAF Osservatorio Astronomico di Roma, Monte Porzio Catone, Italy. [23]Space Science Data Center, Agenzia Spaziale Italiana, Rome, Italy. [24]Dipartimento di Matematica e Fisica, Università degli Studi Roma Tre, Rome, Italy. [25]Istituto Nazionale di Fisica Nucleare, Sezione di Torino, Turin, Italy. [26]Dipartimento di Fisica, Università degli Studi di Torino, Turin, Italy. [27]ASI, Agenzia Spaziale Italiana, Rome, Italy. [28]Science and Technology Institute, Universities Space Research Association, Huntsville, AL, USA. [29]Istituto Nazionale di Fisica Nucleare, Sezione di Roma 'Tor Vergata', Rome, Italy. [30]Institut für Astronomie und Astrophysik, Universität Tübingen, Tübingen, Germany. [31]Astronomical Institute of the Czech Academy of Sciences, Praha 4, Czech Republic. [32]Department of Physics and Astronomy and Space Science Center, University of New Hampshire, Durham, NH, USA. [33]California Institute of Technology, Pasadena, CA, USA. [34]Osaka University, Suita, Japan. [35]International Center for Hadron Astrophysics, Chiba University, Chiba, Japan. [36]Institute for Astrophysical Research, Boston University, Boston, MA, USA. [37]Department of Astrophysics, St. Petersburg State University, Petrodvoretz, Russia. [38]Department of Physics and Astronomy, University of Iowa, Iowa City, IA, USA. [39]Physics Department and McDonnell Center for the Space Sciences, Washington University in St. Louis, St. Louis, MO, USA. [40]Finnish Centre for Astronomy with ESO, University of Turku, Turku, Finland. [41]Université de Strasbourg, CNRS, Observatoire Astronomique de Strasbourg, Strasbourg, France. [42]Graduate School of Science, Division of Particle and Astrophysical Science, Nagoya University, Nagoya, Japan. [43]Department of Physics, The University of Hong Kong, Pokfulam, Hong Kong. [44]Department of Astronomy and Astrophysics, Pennsylvania State University, Pennsylvania, PA, USA. [45]Université Grenoble Alpes, CNRS, IPAG, Grenoble, France. [46]Department of Physics and Astronomy, University of Turku, Turku, Finland. [47]INAF Osservatorio Astronomico di Brera, Merate, Italy. [48]Dipartimento di Fisica e Astronomia, Università degli Studi di Padova, Padua, Italy. [49]Dipartimento di Fisica, Università degli Studi di Roma 'Tor Vergata', Rome, Italy. [50]Mullard Space Science Laboratory, University College London Holmbury St. Mary, Dorking, UK. [51]Anton Pannekoek Institute for Astronomy and GRAPPA, University of Amsterdam, Amsterdam, the Netherlands. ✉e-mail: niccolo.bucciantini@inaf.it